TITLE:

Enhanced Photocatalytic Activity of BiVO4/Bi2S3/SnS2 Heterojunction under Visible Light

AUTHOR(S):

Meng, Sopheak; Ogawa, Takaya; Okumura, Hideyuki; Ishihara, Keiichi N.

京都大学学術情報リポジトリ
KURENAI 紅
Kyoto University Research Information Repository

京都大学
KYOTO UNIVERSITY

KURENAI 紅
京都大学学術情報リポジトリ
Kyoto University Research Information Repository

catalysts

MDPI

Article

Enhanced Photocatalytic Activity of BiVO$_4$/Bi$_2$S$_3$/SnS$_2$ Heterojunction under Visible Light

Sopheak Meng *[ID], Takaya Ogawa[ID], Hideyuki Okumura and Keiichi N. Ishihara *

Graduate School of Energy Science, Kyoto University, Kyoto 606-8501, Japan;
ogawa.takaya.8s@kyoto-u.ac.jp (T.O.); okumura@energy.kyoto-u.ac.jp (H.O.)
* Correspondence: sopheak@social-system.energy.kyoto-u.ac.jp (S.M.); ishihara@energy.kyoto-u.ac.jp (K.N.I.)

check for updates

Abstract: Heterojunction photocatalysts have attracted a significant amount of attention due to their advantages over a single photocatalyst and, particularly, their superior spatial charge separation. Herein, the BiVO$_4$/Bi$_2$S$_3$/SnS$_2$ heterojunction was synthesized via solvothermal synthesis with different ratios of BiVO$_4$ to SnS$_2$. The photodegradation rate of the 0.03 BiVO$_4$/SnS$_2$ sample for rhodamine B removal is 2.3 times or 2.9 times greater than that of a single SnS$_2$ or BiVO$_4$, respectively. The chemical bond between photocatalysts is confirmed by X-ray photoelectron spectroscopy (XPS), and the synchronized shift observed in binding energies strongly indicates the electron screening effect at the heterojunction. A Z-scheme model is proposed to explain charge transfer pathway in the system, in which the formation of Bi$_2$S$_3$ plays a crucial role in the enhanced photocatalytic performance of the heterojunction.

Keywords: BiVO$_4$/Bi$_2$S$_3$/SnS$_2$ heterojunction; visible light; Z-scheme

1. Introduction

In recent years, a tremendous effort has been made to develop efficient photocatalysts due to their potential applications in water splitting [1–3], CO$_2$ reduction [4,5], and pollutant removal [6–8]. A good photocatalyst needs a suitable bandgap to work in the visible light region, in addition to satisfying other important criteria, e.g., abundance, low cost, nontoxicity, low electron–hole recombination rate, and stability. Photocatalysts such as SnS$_2$ and BiVO$_4$ fit most of these conditions; in particular, they can absorb visible light because their bandgaps are 2.18–2.4 eV [1,9]. Although both materials have many advantages as a single photocatalyst, incorporating them with different photocatalysts to form a heterojunction has proved very effective to attain superior photocatalytic activity [1,10–12]. The interface can act as a bridge allowing electrons to migrate between photocatalysts, which, in turn, suppress the photoinduced electron–hole recombination and improve the performance of photocatalysts [11,13]. In addition, the heterojunction may also induce a Z-scheme system in which the redox ability is enhanced via coupling two or more narrow-bandgap semiconductors [1,14].

To date, no attempt has been made to fabricate the BiVO$_4$/SnS$_2$ heterojunction despite many publications on SnS$_2$ and BiVO$_4$ [7,15]. One of the reasons for this could be an occurrence of the reaction between Bi^{3+} and S^{2-} that leads to formation of Bi$_2$S$_3$ at elevated temperatures [6,16]. It would be challenging to obtain a BiVO$_4$/SnS$_2$ heterojunction without formation of Bi$_2$S$_3$. However, the composites containing Bi$_2$S$_3$, such as Bi$_2$S$_3$/ZnS [17], Bi$_2$S$_3$/MoS$_2$ [5,18], and TiO$_2$/Bi$_2$S$_3$ [3], have been shown to promote the photocatalytic activity. Furthermore, earlier researchers have demonstrated that both SnS$_2$ and BiVO$_4$ were successfully fabricated with Bi$_2$S$_3$ to produce Bi$_2$S$_3$/SnS$_2$ and Bi$_2$S$_3$/BiVO$_4$, respectively, exhibiting enhanced photocatalytic performance in dye degradation [15,19–21]. Additionally, ternary heterojunction based on Bi$_2$S$_3$ (e.g., Bi$_2$O$_3$/Bi$_2$S$_3$/MoS$_2$ [2], Bi$_2$S$_3$/SnS$_2$/Bi$_2$O$_3$ [6], and Bi$_2$O$_3$/Bi$_2$S$_3$/MoS$_2$ [16]) have also been proven to improve the photocatalytic

activity. Therefore, viewed from a different perspective, Bi_2S_3 formation from the reaction between SnS_2 and $BiVO_4$ might enhance photocatalytic performance of the composite via formation of a ternary heterojunction.

In this study, the $BiVO_4/Bi_2S_3/SnS_2$ heterojunction was thus synthesized by combining SnS_2 and $BiVO_4$ via ultrasonic mixing and solvothermal synthesis. The formation of Bi_2S_3 during the synthesis would then constitute a ternary heterojunction with SnS_2 and $BiVO_4$. Various molar ratios of $BiVO_4$ to SnS_2 were prepared to investigate the properties of three-phase photocatalysts ($BiVO_4$, Bi_2S_3, and SnS_2) and to optimize the amount of $BiVO_4$ in the composite. Photocatalytic performance of the composite was compared with pure $BiVO_4$ and SnS_2, and the charge transfer pathway in the heterojunction system was examined. A Z-scheme model was then proposed to consistently explain the enhanced photocatalytic activity of $BiVO_4/Bi_2S_3/SnS_2$ heterojunctions.

2. Results and Discussions

2.1. Crystal Structure of the Samples

The crystalline phases of as-prepared samples with different ratios of $BiVO_4$ to SnS_2 were investigated through XRD (X-ray diffraction) patterns as shown in Figure 1. The characteristic peaks at 14.9°, 28.3°, 32.3°, 49.5°, and 52.4° correspond to (001), (100), (101), (110), and (111) planes of hexagonal SnS_2, respectively (ICDD PDF No. 00-023-0677). Other visible peaks can be observed at 18.7°, 19.0°, 28.8°, and 30.5°, assigned to (110), (011), ($\bar{1}$21), and (040) planes of monoclinic $BiVO_4$, respectively (ICDD PDF No. 00-014-0688). In addition to these obvious peaks, there are four small peaks at 22.3°, 23.6°, 24.9°, and 25.2°, which can be assigned to (202), (101), (130), and (310) planes of orthorhombic Bi_2S_3, respectively (ICDD PDF No. 01-089-8965). The XRD patterns of individual synthesized materials ($BiVO_4$, SnS_2, and Bi_2S_3) are shown in Figure S1. These characteristic diffraction peaks confirm three crystal phases of SnS_2, B_2S_3, and $BiVO_4$ in the composites. As the content of $BiVO_4$ during the synthesis is reduced, the diffraction intensities of $BiVO_4$ and Bi_2S_3 decrease and almost disappear for the 0.01 $BiVO_4/SnS_2$ sample due to the very low content of $BiVO_4$ and Bi_2S_3 in the composite. According to the result, the content of Bi_2S_3 depends on the initial concentration of $BiVO_4$ during the hydrothermal synthesis.
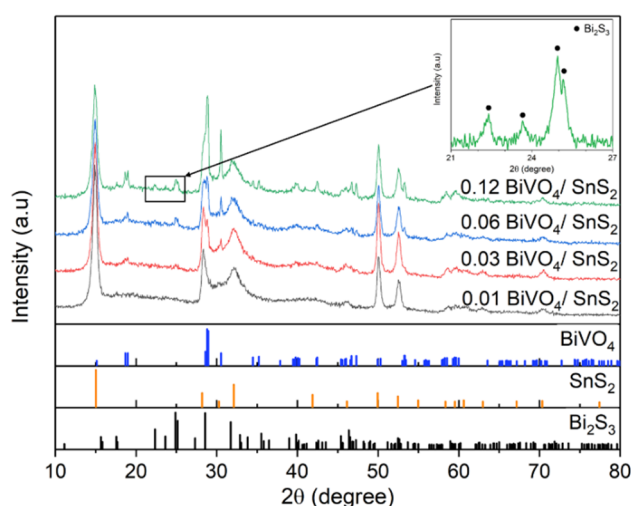
Figure 1. XRD pattern of $BiVO_4/SnS_2$ samples with various ratios of $BiVO_4$ and SnS_2.

2.2. Morphology and Microstructure of the Samples

Figure 2a,b reveals agglomerates of SnS_2 that were composed of ultrafine nanoparticles with diameter of approximately 50 nm. On the other hand, $BiVO_4$ exhibits micron-sized polyhedral particles with a smooth surface, i.e., particular features of microcrystals with many facets, as observed in

Figure 2c. The ultrafine nanoparticles of SnS_2 and microparticles of $BiVO_4$ explain a large difference (more than 100 times) in the specific surface area of SnS_2 and $BiVO_4$ in Table 1. Furthermore, Figure 2d shows a micrograph image of the 0.03 $BiVO_4/SnS_2$ composite, in which the nanoparticles of SnS_2 are attached to, and cover, the particles of $BiVO_4$. Based on the EDS elemental mapping of 0.03 $BiVO_4/SnS_2$ in Figure 3, the elements of Sn, S, Bi, V, and O are uniformly dispersed in the composite, indicating good distribution of $BiVO_4$ and SnS_2 after the incorporation.
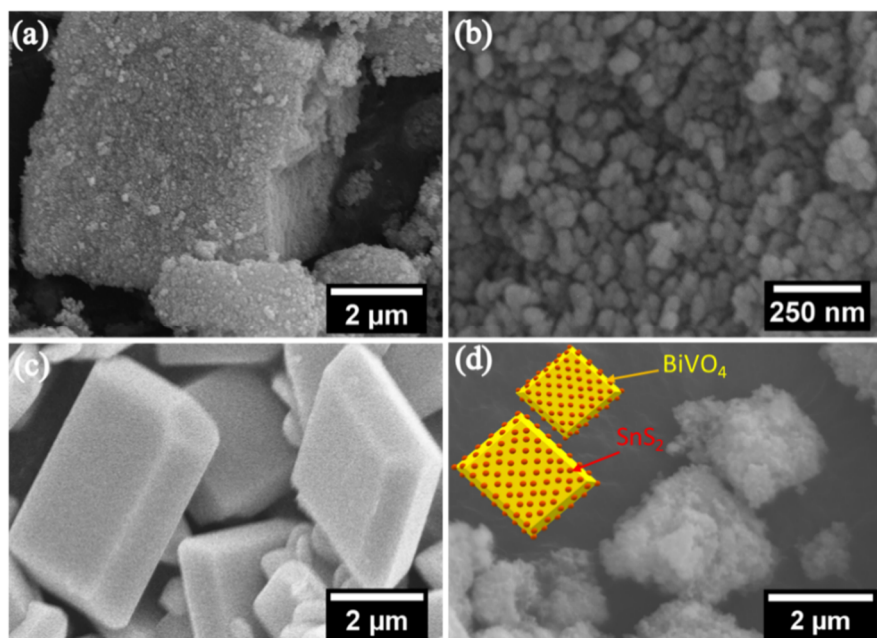
Figure 2. FE-SEM micrographs of (**a**) SnS_2, (**b**) magnified image of SnS_2, (**c**) $BiVO_4$, and (**d**) 0.03 $BiVO_4/SnS_2$ with schematic illustration.

Table 1. Comparison of molar/weight percent $BiVO_4$, specific surface area, and pseudo-first-order-kinetic degradation constant, for SnS_2, $BiVO_4$, and $BiVO_4/SnS_2$ composites with various $BiVO_4$-to-SnS_2 ratios.

| Sample	Molar Percent of $BiVO_4$ (mole %)	Weight Percent of $BiVO_4$ (wt %)	BET Specific Surface Area (m^2/g)	Degradation Rate Constant k (10^{-3} min^{-1})	R^2
SnS_2	0	0	75.7	0.60	0.9408
0.01 $BiVO_4/SnS_2$	0.99	1.74	83.3	1.40	0.9990
0.03 $BiVO_4/SnS_2$	2.91	5.05	74.7	1.60	0.9975
0.06 $BiVO_4/SnS_2$	5.66	9.60	68.5	1.25	0.9965
0.12 $BiVO_4/SnS_2$	10.71	17.53	56.3	0.68	0.9955
$BiVO_4$	100	100	0.6	0.55	0.9625
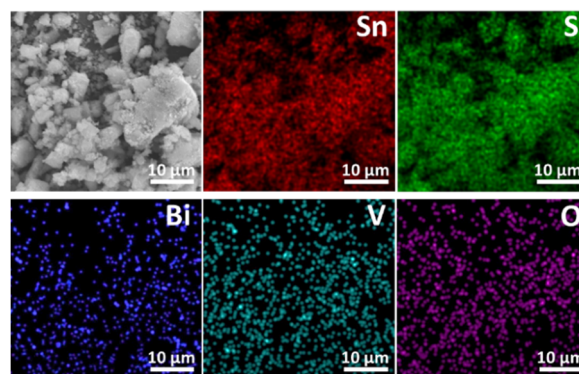
Figure 3. EDS elemental mapping of Sn, S, Bi, V, and O elements in 0.03 $BiVO_4/SnS_2$.

2.3. Optical Absorption Properties

UV–Vis diffuse reflectance spectra (DRS) were used to study optical properties of as-prepared samples. The reflectance spectra were converted to absorption spectra via the Kubelka–Munk function as shown below, in Equation (1) [19,22]:

$$F(R) = \alpha/S = (1 - R)^2/2R, \tag{1}$$

where $F(R)$, α, S, and R are the Kubelka–Munk function, absorption coefficient, scattering coefficient, and reflectance, respectively. As illustrated in Figure 4a, all composites exhibit absorption edges around the wavelength of 550 nm, indicating that they are photoactive in the visible light region. The curves of 0.06 $BiVO_4/SnS_2$ and 0.12 $BiVO_4/SnS_2$ are noticeably different from the remainder as their absorption regions extend beyond 550 nm. This could be attributed to an increase in the content of Bi_2S_3 in the composite.
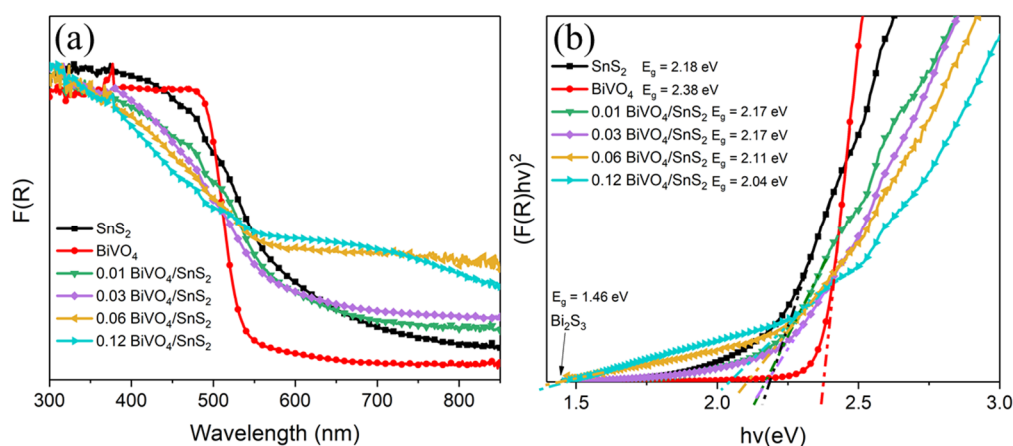
Figure 4. (**a**) UV–Vis diffuse reflectance spectra and (**b**) $(F(R)h\upsilon)^2$ vs. $h\upsilon$ plot of SnS_2, $BiVO_4$, and the $BiVO_4/SnS_2$ composites with various ratios of $BiVO_4$.

The bandgaps (E_g) can be estimated using the following formula:

$$\alpha h\upsilon = B(h\upsilon - E_g)^{n/2}, \tag{2}$$

where $h\upsilon$ and B are incident photon energy and a constant associated with the material, respectively. The coefficient α can be obtained via the Kubelka–Munk function from Equation (1). The $F(R)$ is commonly used to replace α in the Tauc plot $((\alpha h\upsilon)^{2/n}$ vs. $h\upsilon)$ [11,19,23]. In addition, SnS_2, Bi_2S_3, and $BiVO_4$ have been reported to be direct transition semiconductors, thus n = 1 is used in the equation [19,24]. Thus, the $(F(R)h\upsilon)^2$ vs. $h\upsilon$ graph can be plotted as in Figure 4b, and the E_g values are evaluated by extrapolating the linear part of the curve to intercept the $F(R) = 0$ line. The E_g values of $BiVO_4$, SnS_2, and Bi_2S_3 are accordingly estimated to be 2.38, 2.18, and 1.46 eV, respectively, which are similar to those in previous reports [22,25]. In addition, the effective E_g values of 0.01 $BiVO_4/SnS_2$, 0.03 $BiVO_4/SnS_2$, 0.06 $BiVO_4/SnS_2$, and 0.12 $BiVO_4/SnS_2$ are estimated to be 2.17, 2.17, 2.11, and 2.04 eV, respectively. It appears that the apparent E_g value of the composite is decreased with an increase in $BiVO_4$. This bandgap modification may be ascribed to small composition variation of SnS_2, $BiVO_4$, and Bi_2S_3, especially near the interface. This phenomenon is also reported in previous publications [3,16,19].

2.4. X-Ray Photoelectron Spectroscopy (XPS)

The XPS survey spectrum of 0.03 $BiVO_4/SnS_2$ composite is shown in Figure 5a, demonstrating that it consists of Sn, S, Bi, V, and O elements in agreement with the EDS result. The chemical state of each element, investigated via the high-resolution XPS analyses, is shown in Figure 5b,c. As observed

in Figure 5b, two separate spectra with peaks at 494.89 and 486.49 eV with an energy difference of 8.4 eV correspond to Sn $3d_{3/2}$ and Sn $3d_{5/2}$ of Sn^{4+}, respectively, for a common SnS_2 [4,10,19]. On the other hand, for the 0.03 $BiVO_4/SnS_2$ composite, it is noted that both Sn 3d peaks shift to the higher binding energy side by about 0.30–0.35 eV, compared with those of pure SnS_2. The blueshift observed in the Sn 3d spectra is also found in, and synchronous with, the S 2p spectra.
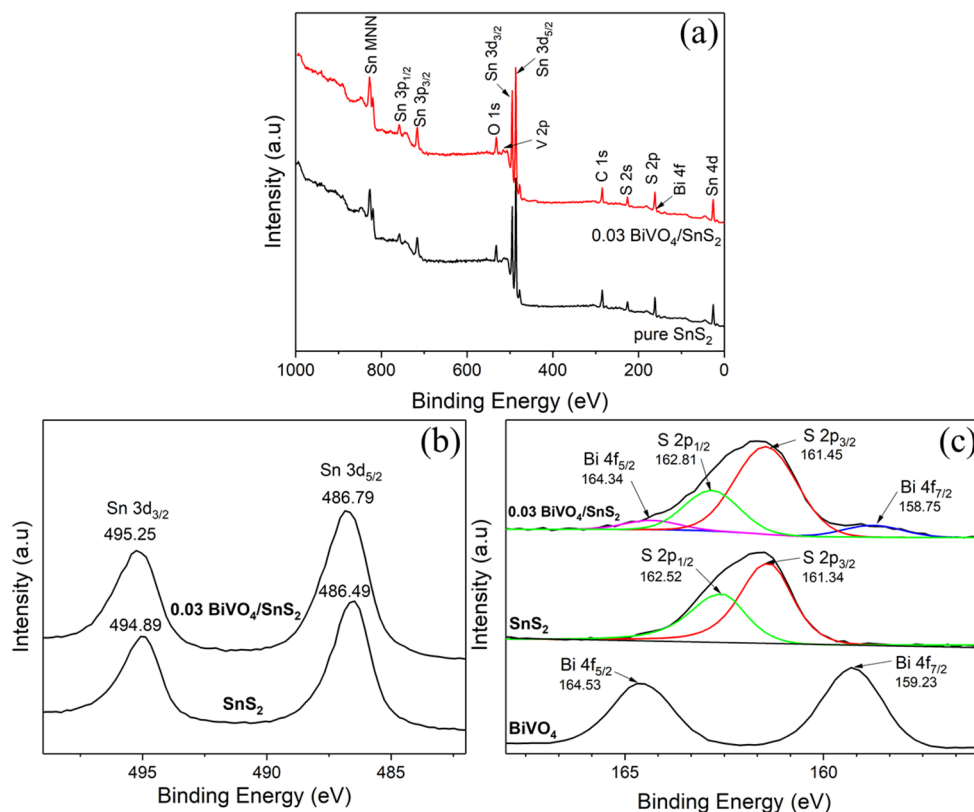
Figure 5. (**a**) XPS survey spectra of 0.03 $BiVO_4/SnS_2$ and pure SnS_2 and high-resolution XPS spectra of (**b**) Sn 3d orbital and (**c**) Bi 4f and S 2p orbital.

As shown in Figure 5c, the S $2p_{3/2}$ (161.34 eV) and S $2p_{1/2}$ (162.52 eV) peaks, corresponding to typical Sn-S bonds of pure SnS_2 [4,9,10], also exhibit a blueshift in the binding energy by 0.1–0.3 eV for the 0.03 $BiVO_4/SnS_2$ composite. Furthermore, the synchronized binding energy shift is also observed, with an opposite direction, for the Bi 4f spectra. The spectral peaks for the 0.03 $BiVO_4/SnS_2$ composite at 158.75 and 164.34 eV, which belong to Bi $4f_{7/2}$ and Bi $4f_{5/2}$ of $BiVO_4$, respectively, exhibit the redshift, by 0.2–0.5 eV, compared with Bi 4f peaks (159.23 and 164.53 eV) of pure $BiVO_4$ [15]. Importantly, the synchronous phenomena are reproducible.

The shift of binding energy in the core-level of XPS spectra should be largely attributed to the change in electron concentration of semiconductors due to the interaction between SnS_2 and $BiVO_4$ [26]. As the electron concentration decreases, the binding energy of the semiconductor increases, and vice versa, due to the so-called electron screening effect [27]. When a heterojunction is formed through chemical interaction, the Fermi energy levels of both materials are adjusted, allowing the electron transfer between materials to achieve equilibrium [10,26,27]. In the case of the 0.03 $BiVO_4/SnS_2$ composite, it implies that SnS_2 has a higher Fermi energy level than that of $BiVO_4$, thus the electron migrates from SnS_2 to $BiVO_4$. This consequently reduces the electron concentration of SnS_2 and increases that of $BiVO_4$. As a result, the Sn 3d and S 2p spectra of the composite exhibit the blueshift, while Bi 4f spectra exhibit the redshift.

Furthermore, the broad peaks of the Bi 4f exhibited in the 0.03 $BiVO_4/SnS_2$ composite may be caused by the presence of Bi_2S_3. The Bi $4f_{7/2}$ and Bi $4f_{5/2}$ spectral peaks of a typical Bi_2S_3 are

reported to be at 158.4 and 163.8 eV [28], respectively, which are slightly lower than those of $BiVO_4$. Moreover, the S 2p peaks at 161.45 and 162.81 eV in the 0.03 $BiVO_4/SnS_2$ composite could also correspond to S^{2-} of Bi_2S_3 [29]. The results from XPS spectra and XRD patterns (Section 2.1) strongly suggest the coexistence of SnS_2, Bi_2S_3, and $BiVO_4$ in the composite. Additionally, the shifts in binding energy indicate that the interaction among SnS_2, Bi_2S_3, and $BiVO_4$ in the 0.03 $BiVO_4/SnS_2$ composite is a chemical bonding rather than a physical contact only.

2.5. Photocatalytic Activity

Photocatalytic activity was evaluated via concentration reduction in RhB (rhodamine B) dye solution over time, as shown in Figure 6a, where C_0 is the initial RhB concentration at the time of light irradiation (t = 0), and C_t is the RhB concentration at any sampling time during irradiation. Blank RhB (a control test) in Figure 6a demonstrates that the RhB dye solution was stable under this test condition without any photocatalyst in the solution and that the photolysis of RhB dye was negligible over 240 min of visible light irradiation. Conversely, the concentration of RhB decreased over time for all other RhB solutions containing any photocatalyst, evidencing that photocatalysts used in this study respond to visible light (λ > 420 nm). Importantly, all composited powders exhibit higher photocatalytic degradation of RhB than that of bare SnS_2, Bi_2S_3, or $BiVO_4$ under visible light irradiation for over 240 min. The temporal evolution of RhB absorption spectra for each photocatalyst can be seen in Figure S2.
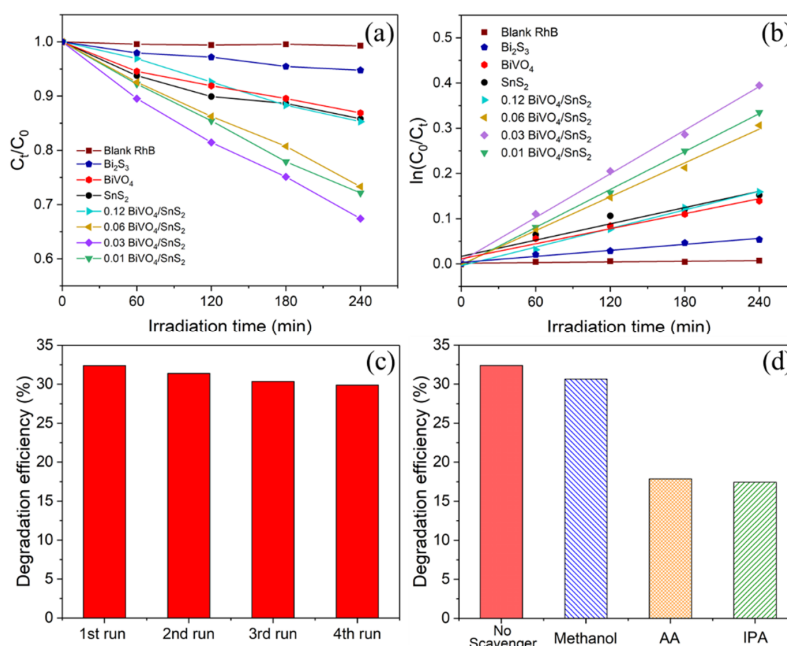
Figure 6. (**a**) Photocatalytic RhB degradation for various photocatalysts; (**b**) pseudo-first-order-kinetics for RhB photodegradation; (**c**) RhB degradation efficiency of 0.03 $BiVO_4/SnS_2$ over four cycles; and (**d**) the effect of methanol, ascorbic acid (AA), and isopropyl alcohol (IPA) on RhB photodegradation by 0.03 $BiVO_4/SnS_2$ under visible light irradiation (λ > 420 nm) for 240 min.

The degradation rates were compared using a photodegradation rate constant (k), assuming a pseudo-first-order reaction model, $\ln(C_0/C_t) = kt$, as shown in Figure 6b. The kinetic model fits the data well, and the k value of the 0.03 $BiVO_4/SnS_2$ sample is about 2.3 times or 2.9 times greater than that of single SnS_2 or $BiVO_4$, respectively (Table 1). The photocatalytic activity of the composite is enhanced as the content of $BiVO_4$ is increased from 0.01 to 0.03, whereas further addition of $BiVO_4$ leads to reduction in photocatalytic activity of the composites (0.06 $BiVO_4/SnS_2$ and 0.12 $BiVO_4/SnS_2$). It is thus reasonable to consider that an optimal molar ratio exists at a relatively low concentration of $BiVO_4$. One possible

reason could be the variation in the "effective" specific surface area. As shown in Table 1, the specific surface area of the composites mostly decreases with an addition of $BiVO_4$, ascribed to the significantly small value of bare $BiVO_4$ (0.6 m^2/g). Furthermore, the interfacial reaction and agglomeration of powders may affect the effective active area for photocatalytic activity. As previously mentioned, the formation of Bi_2S_3 is intensive as the amount of $BiVO_4$ in the composite is increased. Although a small amount of Bi_2S_3 would be favorable for the composite, excess content may lead to deterioration of the photocatalytic performance because Bi_2S_3 has low photocatalytic activity of RhB degradation compared to SnS_2 and $BiVO_4$, possibly due to its rapid recombination rate of the photogenerated electron-hole [17]. Thus, excessive Bi_2S_3 could act as a recombination center for electron-hole pairs in the composite, which is similar to the findings of previous studies [13,19].

In addition to the photocatalytic activity of the material, stability and reusability are also important to determine its value in practical applications. Thus, the reusability test was also conducted by collecting the used sample (0.03 $BiVO_4$/SnS_2) after irradiation via centrifuge and putting it back into the fresh RhB solution. The same procedure for the photocatalytic activity measurement was repeated in this reusability test. Figure 6c shows the degradation efficiencies of 0.03 $BiVO_4$/SnS_2 composite over four cycles, illustrating stability and reusability of the 0.03 $BiVO_4$/SnS_2 composite. A slight loss (around 6%) of the degradation efficiency in the 4th run could be due to a loss of photocatalyst during the recovery process. Furthermore, the stability of the composite was also confirmed by XRD pattern before and after irradiation (Figure S3), in which the crystal structure of 0.03 $BiVO_4$/SnS_2 was not significantly altered after RhB degradation process.

To determine main reactive species responsible for RhB photodegradation by 0.03 $BiVO_4$/SnS_2 during irradiation, scavenger tests were conducted using various types of scavengers. In this study, methanol (10 mM) [6], ascorbic acid (AA, 10 mM) [30], and isopropyl alcohol (IPA, 10 mM) [16] were used as the scavengers for superoxide radicals ($\bullet O_2^-$), holes (h$^+$), and hydroxyl radicals ($\bullet OH$), respectively. As shown in Figure 6d, an addition of methanol into the system has only a slight effect on RhB degradation, indicating that $\bullet O_2^-$ radicals play a minor role in the degradation process. Conversely, AA (h$^+$ scavenger) and IPA ($\bullet OH$ scavenger) greatly suppress photocatalytic RhB degradation. The result strongly suggests that h$^+$ and $\bullet OH$ radicals are the main reactive species for the RhB photodegradation process with the 0.03 $BiVO_4$/SnS_2 photocatalyst under visible light ($\lambda > 420$ nm) irradiation.

2.6. Possible Mechanism for Photocatalytic Activity Enhancement of BiVO₄/Bi₂S₃/SnS₂ Heterojunction

A plausible photocatalytic mechanism of the $BiVO_4$/Bi_2S_3/SnS_2 heterojunction could be explained by understanding the band energy structures of the photocatalysts as illustrated in Figure 7. The empirical Equations (3) and (4) are often used to estimate the band edge of the semiconductor such as conduction band edge potential (E_{CB}) and valence band edge potential (E_{VB}) [15,19]:

$$E_{VB} = \chi - E^e + 0.5E_g \tag{3}$$

$$E_{CB} = E_{VB} - E_g, \tag{4}$$

where, χ is absolute electronegativity of a semiconductor, determined by the geometric mean of absolute electronegativity values of constituent atoms. In this study (Section 2.3), E_g values of SnS_2, Bi_2S_3, and $BiVO_4$ are 2.18, 1.46, and 2.38 eV, respectively. The absolute electronegativity values of Bi, V, O, Sn, and S are 4.69, 3.6, 7.54, 4.3, and 6.22 eV, respectively, taken from Pearson's experimental data [31]. The value E^e is the energy of the free electron on the hydrogen scale, which is 4.5 eV. According to this calculation, E_{CB} and E_{VB} of SnS_2 are estimated to be −0.09 and 2.09 eV, respectively, whereas $BiVO_4$ exhibits E_{CB} of 0.47 eV and E_{VB} of 2.85 eV, and Bi_2S_3 possesses E_{CB} of 0.05 eV and E_{VB} of 1.51 eV. The E_{CB} and E_{VB} values of these photocatalysts in the present study are similar to those of previous reports [11,16,19].
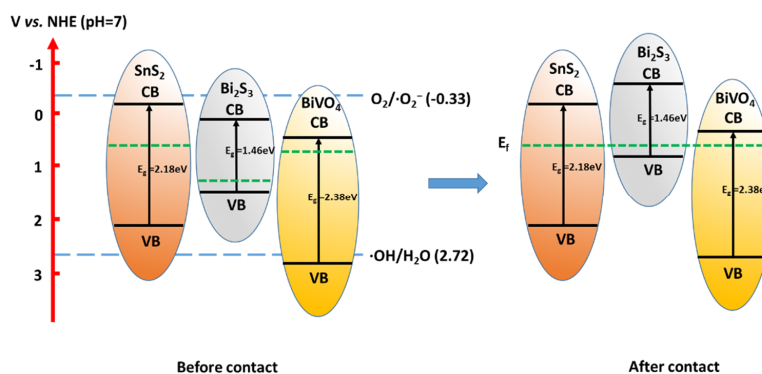
Figure 7. Band energy structures of $BiVO_4$, Bi_2S_3, and SnS_2 before and after contact.

Fermi level positions of SnS_2, Bi_2S_3, and $BiVO_4$ with respect to their VBs (valence bands) can be determined from the potential difference between VBM (VB maximum) and Fermi level from the valence band XPS spectra in Figure S4 [12]. The difference between the Fermi level and VBMs of SnS_2, Bi_2S_3, and $BiVO_4$ is found to be 1.3, 0.3, and 2 eV, respectively. The result indicates that SnS_2 and $BiVO_4$ are n-type semiconductors, whereas Bi_2S_3 is a p-type semiconductor, which is in agreement with prior studies [2,6,16]. Our XPS results suggest that the photocatalysts are chemically bonded at the interface, and their Fermi levels are aligned after contact; as a result, their band energy structures are accordingly adjusted, creating a heterojunction as depicted in Figure 7 [12,16].

To understand the charge-transfer pathway in the $BiVO_4/Bi_2S_3/SnS_2$ heterojunction system, we explore and examine two possible models for the charge transfer process as proposed in Figure 8. All of the photocatalysts in both models are capable of generating electron-hole pairs upon visible light illumination due to their narrow bandgaps. In model A, the photogenerated electrons (e^-) would migrate from the CB (conduction band) of Bi_2S_3 to CBs of SnS_2 and $BiVO_4$. Thus, $\bullet O_2^-$ radicals would not be produced by the heterojunction since the CBs of both SnS_2 and $BiVO_4$ are incapable of reducing dissolved O_2 to produce $\bullet O_2^-$ because their CBs are less negative than -0.33 eV ($O_2/\bullet O_2^-$) [16]. On the other hand, the generated holes (h^+) would move from the VBs of both SnS_2 and $BiVO_4$ to the VB of Bi_2S_3. In this scenario, the heterojunction also could not oxidize H_2O to form $\bullet OH$ because VB of Bi_2S_3 is less positive than 2.72 eV (for $\bullet OH/H_2O$) [8,16]. It has been reported that $\bullet O_2^-$, $\bullet OH$, and h^+ play major roles in the RhB photodegradation process [16,32,33]. Although model A might improve charge separation of photoinduced electrons and holes, it would be less efficient as the composite would be unable to produce $\bullet O_2^-$ and $\bullet OH$ to degrade the RhB dye. Moreover, the model is inconsistent with our trapping experiment (our scavenger test in Section 2.5) in which $\bullet O_2^-$ and $\bullet OH$ were observed in the RhB degradation process.

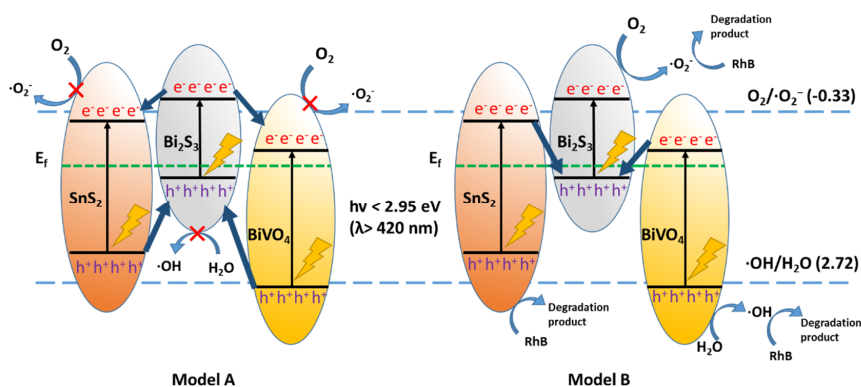**Figure 8.** Proposed charge-transfer pathway models and RhB degradation mechanism of $BiVO_4/Bi_2S_3/SnS_2$ under visible light illumination.

A more plausible scenario might be that of model B in Figure 8, involving a Z-scheme process. Based on this model, we can explain the presence of $\bullet O_2^-$, $\bullet OH$, and h^+ for the RhB degradation process. In the Z-scheme process, the photoinduced e^- from the CBs of both SnS_2 and $BiVO_4$ could migrate to and recombine with h^+ in the VB of Bi_2S_3. Consequently, e^- from the CB of Bi_2S_3 would be able to react and reduce the dissolved O_2 in H_2O to produce $\bullet O_2^-$ because the CB of Bi_2S_3 is more negative than -0.33 eV. According to our scavenger test, $\bullet O_2^-$ played only a minor role in the RhB degradation process by the 0.03 $BiVO_4/SnS_2$ heterojunction, which fits well with the current model due to the low optimal content of Bi_2S_3 in the composite. Meanwhile, since h^+ in the VB of Bi_2S_3 quickly recombine with e^- of $BiVO_4$ and SnS_2, it would leave h^+ in the VB of $BiVO_4$ to oxidize H_2O and generate $\bullet OH$ (2.72 vs. NHE); similarly, h^+ are also left behind in the VB of SnS_2. As the VB of SnS_2 is not negative enough to produce $\bullet OH$, h^+ would decompose RhB directly due to its strong oxidation ability [16,32]. Thus, the Z-scheme model is consistent with the experimental result, and may be used to explain the charge-transfer pathway of the $BiVO_4/Bi_2S_3/SnS_2$ heterojunction system.

3. Materials and Methods

3.1. Materials

Thioacetamide (C_2H_5NS, 98%), acetic acid (CH_3COOH, 99.7%), ethylene glycol (($CH_2OH)_2$, 99.5%), L-ascorbic acid ($C_6H_8O_6$, 99.6%), and thiourea (H_2NCSNH_2, 98%) were purchased from FUJIFILM Wako Pure Chemical Corporation (Osaka, Japan). The tin(IV) chloride pentahydrate ($SnCl_4\cdot5H_2O$, 98%), ammonium vanadate (V) (NH_4VO_3, 99.0%), bismuth (III) nitrate pentahydrate ($Bi(NO_3)_3\cdot 5H_2O$ 99.5%), methanol (CH_3OH, 99.8%), and isopropyl alcohol (($CH_3)_2CHOH$, 99.7%) were supplied by Nacalai Tesque (Kyoto, Japan). The rhodamine B ($C_{28}H_{31}ClN_2O_3$, > 95%) was purchased from Tokyo Chemical Industry (Tokyo, Japan). All chemicals were analytical grade and used without further purification. Deionized water (DI water) was obtained from the Direct-Q water purification system (Millipore).

3.2. Preparation of SnS$_2$

Preparation of SnS_2 was conducted via a typical synthesis method. The powder of $SnCl_4\cdot5H_2O$ (5 mmol) was dissolved in 40 mL of 5% (v/v%) acetic acids under magnetic stirring. Then, 10 mmol amount of thioacetamide was added to the solution. After 30 min of vigorous stirring to achieve a homogeneous solution, the solution was transferred to a stainless-steel autoclave attached with a Teflon liner to fill 80% of its maximum capacity (50 mL). It was then put in a preheat electric oven at 150 °C for 12 h under autogenous pressure. After letting the autoclave cool to room temperature, SnS_2 precipitate was collected via centrifuge at 4000 rpm for 5 min. The SnS_2 was then washed several times with DI water and ethanol and dried at 90 °C overnight.

3.3. Preparation of BiVO$_4$

Typical hydrothermal synthesis was used to prepare $BiVO_4$. The first solution was prepared by dissolving 2.43 g of $Bi(NO_3)_3\cdot5H_2O$ in 20 mL of 2 M HNO_3 acid, and the second solution was made by dissolving an equimolar amount of NH_4VO_3 in 2 M NaOH solution. Then, the second solution was poured drop by drop into the first solution. The clear solution turned yellow as $BiVO_4$ precipitate was formed. The mixture solution was continually stirred for another 10 min before adding 1 mL of acetic acid into the solution. After 1 h of stirring, the solution was transferred to the stainless-steel autoclave with a Teflon liner. The autoclave was heated at 180 °C for 24 h. Finally, $BiVO_4$ precipitate was collected, washed, and dried, following the same procedure described in Section 3.2.

3.4. Preparation of BiVO$_4$/Bi$_2$S$_3$/SnS$_2$ Composites

The composite was prepared using an ultrasonic mixing and a solvothermal synthesis. A specific amount of $BiVO_4$ (0.01, 0.03, 0.06, and 0.12 mmol) was mixed with 1 mmol of SnS_2 in 40 mL of ethylene glycol. The mixture was thoroughly mixed via ultrasonication at 45 kHz for 1 h before transferring to

the autoclave. It was then sealed and heated at 150 °C for 8 h. The final product of the composite was obtained through washing and drying, following the same procedure as stated in Sections 3.2 and 3.3. The composites with different ratios of $BiVO_4$ to SnS_2 were denoted, respectively, as 0.01 $BiVO_4/SnS_2$, 0.03 $BiVO_4/SnS_2$, 0.06 $BiVO_4/SnS_2$, and 0.12 $BiVO_4/SnS_2$. For reference, a bare Bi_2S_3 was synthesized using solvothermal synthesis (detailed in the Supplementary Information).

3.5. Characterization

X-ray diffraction (XRD) measurement was conducted using a Rigaku RINT2100 at 40 kV and 30 mA with Cu Kα radiation (λ = 1.5418 Å), where the diffractogram was obtained via scanning the sample in a 2θ angle range from 10° to 80°. Microstructures and morphologies of the samples were investigated using an FE-SEM (Hitachi SU6600 Scanning Electron Microscope) equipped with Bruker EDX operated at 15 and 20 kV for SEM and EDX, respectively, where all samples were coated with Au via sputtering prior to the analyses. UV–Vis diffuse reflectance spectra (DRS) were obtained using a Lambda 750S UV/Vis/NIR Spectrophotometer with $BaSO_4$ as reference. X-ray photoelectron spectroscopy (XPS, JPS-9030 X-ray photoelectron spectrometer) was conducted with Mg Kα radiation using C 1s = 284.8 eV as reference. The Brunauer–Emmett–Teller (BET) specific surface area was measured and evaluated using nitrogen gas adsorption with a FlowSorb III 2305 Micromeritics Instrument (Shimadzu, Japan).

3.6. Photocatalytic Activity Measurement

Evaluation of photocatalytic activity was conducted via the photodegradation of RhB dye under visible light irradiation using a 500 W Xe lamp (Ushio, UXL-500D-O) equipped with a cutoff filter (λ > 420 nm). The intensity of light from the Xe lamp was 100 mW/cm^2 calibrated using a Spectroradiometer (S-2440 model II). After passing through the cutoff and water filters, the sample solution received around 40 mW/cm^2 of light intensity. In each measurement process, 30 mg of the photocatalyst was put into 80 mL of RhB solution (5 mg/L, 0.01 mmol/L) in a beaker with 100 mL capacity. The solution was magnetically stirred and maintained at 25 °C during irradiation. About 3 mL of sample solution was taken every 60 min, and the photocatalyst powder was filtered out by syringe filter (0.22 μm, PTFE). The absorbance of each RhB solution was measured using a UV–Vis spectrophotometer (Lambda 750S UV/Vis/NIR). Then, the concentration of RhB was determined from the absorbance intensity at λ_{max} = 554 nm. Before irradiation, the establishment of adsorption–desorption equilibrium between photocatalyst and RhB solution was achieved to ensure an accurate result of photocatalytic activity.

Since SnS_2 exhibits exceptionally strong adsorptivity for RhB dye [23], an initial dye concentration (C_0) for each photocatalytic test would be different, depending on the ratio of $BiVO_4/SnS_2$ composites, after achieving an adsorption–desorption equilibrium. To ensure that all samples had relatively similar initial concentrations at the start of illumination, all samples were subjected to the adsorption–desorption process twice. Each sample was added to a RhB solution, which was then agitated by sonication for 10 min and magnetically stirred for 60 min in the dark. Then, the sample was collected via centrifuge and put into a fresh RhB solution, where the adsorption–desorption procedure was performed again prior to the photocatalytic test. This devised method allowed an initial RhB concentration (C_0) to be similar for each photocatalytic test, using various composite ratios.

4. Conclusions

In summary, three-phase photocatalysts consisting of $BiVO_4$, Bi_2S_3, and SnS_2 were prepared by chemical reaction between $BiVO_4$ and SnS_2 via solvothermal synthesis. The composite photocatalyst produced via a molar ratio of 1:0.03 (SnS_2:$BiVO_4$) demonstrates the highest photocatalytic performance for RhB degradation among our prepared samples. The composite is proved to be stable after several cycles under visible light irradiation. The main reactive species for the photocatalytic degradation of RhB for 0.03 $BiVO_4/SnS_2$ are h$^+$ and •OH, whereas •O$_2{}^-$ also plays a minor role in the degradation

process. The enhanced photocatalytic activity is attributed to the formation of Bi_2S_3, allowing a suitable condition for the electron pathway (Z-scheme) in the $BiVO_4/Bi_2S_3/SnS_2$ heterojunction. We believe that our discovery of the beneficial formation of Bi_2S_3 could encourage more research that focuses on materials prone to reaction with each other at elevated temperature and pressure. The finding may provide a different approach for preparation of ternary heterojunctions by taking advantage of the chemical reaction between combined photocatalysts.

Supplementary Materials: The following are available online at http://www.mdpi.com/2073-4344/10/11/1294/s1, Figure S1: XRD pattern comparison of SnS_2, Bi_2S_3, $BiVO_4$, and 0.12 $BiVO_4/SnS_2$ composite, Figure S2: Absorbance spectra of RhB solution as a function of time during the degradation process under visible light ($\lambda > 420$ nm) in the presence of (**a**) 0.01 $BiVO_4/SnS_2$, (**b**) 0.03 $BiVO_4/SnS_2$, (**c**) 0.06 $BiVO_4/SnS_2$, (**d**) 0.12 $BiVO_4/SnS_2$, (**e**) SnS_2, and (**f**) $BiVO_4$, Figure S3: XRD patterns of 0.03 $BiVO_4/SnS_2$ before and after RhB photodegradation, Figure S4: Valence band XPS spectra of bare $BiVO_4$, Bi_2S_3, and SnS_2.

Author Contributions: Conceptualization, S.M.; methodology, S.M. and H.O.; formal analysis, S.M.; investigation, S.M.; writing—original draft preparation, S.M.; writing—review and editing, T.O. and H.O.; visualization, S.M. and K.N.I.; supervision, K.N.I. All authors have read and agreed to the published version of the manuscript.

Conflicts of Interest: The authors declare no conflict of interest.

References

1. Kumar, N.; Krishnarao, N.; Singh, S.A. Cocatalyst free Z-schematic enhanced H2 evolution over LaVO4/BiVO4 composite photocatalyst using Ag as an electron mediator. *Appl. Catal. B Environ.* **2018**, *220*, 512–523. [CrossRef]
2. Ke, J.; Liu, J.; Sun, H.; Zhang, H.; Duan, X.; Liang, P.; Li, X.; Tade, M.O.; Liu, S.; Wang, S. Facile assembly of Bi2O3/Bi2S3/MoS2 n-p heterojunction with layered n-Bi2O3 and p -MoS2 for enhanced photocatalytic water oxidation and pollutant degradation. *Appl. Catal. B Environ.* **2017**, *200*, 47–55. [CrossRef]
3. Ai, G.; Mo, R.; Chen, Q.; Xu, H.; Yang, S.; Li, H.; Zhong, J. TiO2/Bi2S3 core-shell nanowire arrays for photoelectrochemical hydrogen generation. *RSC Adv.* **2015**, *5*, 13544–13549. [CrossRef]
4. Shown, I.; Samireddi, S.; Chang, Y.C.; Putikam, R.; Chang, P.H.; Sabbah, A.; Fu, F.Y.; Chen, W.F.; Wu, C.I.; Yu, T.Y.; et al. Carbon-doped SnS2 nanostructure as a high-efficiency solar fuel catalyst under visible light. *Nat. Commun.* **2018**, *9*. [CrossRef] [PubMed]
5. Kim, R.; Kim, J.; Do, J.Y.; Seo, M.W.; Kang, M. Carbon Dioxide Photoreduction on the Bi2S3 / MoS2 Catalyst. *Catalysts* **2019**, *18*, 998. [CrossRef]
6. Yu, C.; Wang, K.; Yang, P.; Yang, S.; Lu, C.; Song, Y.; Dong, S.; Sun, J.; Sun, J. One-pot facile synthesis of Bi2S3/SnS2/Bi2O3 ternary heterojunction as advanced double Z-scheme photocatalytic system for efficient dye removal under sunlight irradiation. *Appl. Surf. Sci.* **2017**, *420*, 233–242. [CrossRef]
7. Kgoetlana, C.M.; Malinga, S.P.; Dlamini, L.N. Photocatalytic Degradation of Chlorpyrifos with Mn-WO3/SnS2 Heterostructure. *Catalysts* **2020**, *10*, 699. [CrossRef]
8. Cao, J.; Xu, B.; Lin, H.; Luo, B.; Chen, S. Novel Bi2S3-sensitized BiOCl with highly visible light photocatalytic activity for the removal of rhodamine B. *Catal. Commun.* **2012**, *26*, 204–208. [CrossRef]
9. Lin, C.; Zhu, M.; Zhang, T.; Liu, Y.; Lv, Y.; Li, X.; Liu, M. Cellulose/SnS2 composite with enhanced visible-light photocatalytic activity prepared by microwave-assisted ionic liquid method. *RSC Adv.* **2017**, *7*, 12255–12264. [CrossRef]
10. Zhang, Z.; Shao, C.; Li, X.; Sun, Y.; Zhang, M.; Mu, J.; Zhang, P.; Guo, Z.; Liu, Y. Hierarchical assembly of ultrathin hexagonal SnS2 nanosheets onto electrospun TiO2 nanofibers: Enhanced photocatalytic activity based on photoinduced interfacial charge transfer. *Nanoscale* **2013**, *5*, 606–618. [CrossRef] [PubMed]
11. Zhang, Y.C.; Du, Z.N.; Li, K.W.; Zhang, M.; Dionysiou, D.D. High-performance visible-light-driven SnS2/SnO2 nanocomposite photocatalyst prepared via in situ hydrothermal oxidation of SnS2 nanoparticles. *ACS Appl. Mater. Interfaces* **2011**, *3*, 1528–1537. [CrossRef]

12. Safaei, J.; Ullah, H.; Aida, N.; Firdaus, M.; Noh, M.; Fairus, M.; Tahir, A.A.; Ahmad, N.; Adib, M. Enhanced photoelectrochemical performance of Z-scheme g-C3 N4/BiVO4 photocatalyst. *Appl. Catal. B Environ.* **2018**, *234*, 296–310. [CrossRef]

13. Li, X.; Li, Y.; Shen, J.; Ye, M. A controlled anion exchange strategy to synthesize Bi2S3 nanoparticles/plate-like Bi2WO6 heterostructures with enhanced visible light photocatalytic activities for Rhodamine B. *Ceram. Int.* **2016**, *42*, 3154–3162. [CrossRef]

14. Xu, Q.; Zhang, L.; Yu, J.; Wageh, S.; Al-Ghamdi, A.A.; Jaroniec, M. Direct Z-scheme photocatalysts: Principles, synthesis, and applications. *Mater. Today* **2018**, *21*, 1042–1063. [CrossRef]

15. Ma, D.K.; Guan, M.L.; Liu, S.S.; Zhang, Y.Q.; Zhang, C.W.; He, Y.X.; Huang, S.M. Controlled synthesis of olive-shaped Bi2S3/BiVO4 microspheres through a limited chemical conversion route and enhanced visible-light-responding photocatalytic activity. *Dalt. Trans.* **2012**, *41*, 5581–5586. [CrossRef]

16. Wang, J.; Jin, J.; Wang, X.; Yang, S.; Zhao, Y.; Wu, Y.; Dong, S.; Sun, J.; Sun, J. Facile fabrication of novel BiVO4/Bi2S3/MoS2 n-p heterojunction with enhanced photocatalytic activities towards pollutant degradation under natural sunlight. *J. Colloid Interface Sci.* **2017**, *505*, 805–815. [CrossRef]

17. Wu, Z.; Chen, L.; Xing, C.; Jiang, D.; Xie, J.; Chen, M. Controlled synthesis of Bi2S3/ZnS microspheres by an in situ ion-exchange process with enhanced visible light photocatalytic activity. *J. Chem. Soc. Dalt. Trans.* **2013**, *42*, 12980–12988. [CrossRef]

18. Vattikuti, S.V.P.; Byon, C. Bi2S3 nanorods embedded with MoS2 nanosheets composite for photodegradation of phenol red under visible light irradiation. *Superlattices Microstruct.* **2016**, *100*, 514–525. [CrossRef]

19. Gao, X.; Huang, G.; Gao, H.; Pan, C.; Wang, H.; Yan, J.; Liu, Y.; Qiu, H.; Ma, N.; Gao, J. Facile fabrication of Bi2S3/SnS2 heterojunction photocatalysts with efficient photocatalytic activity under visible light. *J. Alloys Compd.* **2016**, *674*, 98–108. [CrossRef]

20. Ren, L.Z.; Zhang, D.E.; Hao, X.Y.; Xiao, X.; Gong, J.Y.; Wang, M.Y.; Tong, Z.W. Synthesis and photocatalytic performance of Bi2S3/SnS2 heterojunction. *Funct. Mater. Lett.* **2017**, *10*, 3–7. [CrossRef]

21. Zhuang, C.; Tang, L.; Yu, Z.; Peng, T.; Zhang, Y.; Li, L.; Zhou, Y.; Zou, Z. Hollow BiVO4/Bi2S3 cruciate heterostructures with enhanced visible-light photoactivity. *Catal. Sci. Technol.* **2019**, *9*, 182–187. [CrossRef]

22. Zhang, Y.C.; Du, Z.N.; Li, K.W.; Zhang, M. Size-controlled hydrothermal synthesis of SnS2 nanoparticles with high performance in visible light-driven photocatalytic degradation of aqueous methyl orange. *Sep. Purif. Technol.* **2011**, *81*, 101–107. [CrossRef]

23. Zhang, G.; Du, X.; Wang, Y.; Wang, H.; Wang, W.; Fu, Z. Controllable synthesis of SnS2 nanostructures with high adsorption and photocatalytic activities. *Mater. Sci. Semicond. Process.* **2017**, *64*, 77–84. [CrossRef]

24. Walsh, A.; Yan, Y.; Huda, M.N.; Al-Jassim, M.M.; Wei, S.H. Band edge electronic structure of BiVO4: Elucidating the role of the Bi s and V d orbitals. *Chem. Mater.* **2009**, *21*, 547–551. [CrossRef]

25. Chen, H.Q.; Lin, L.Y.; Chen, S.L. Direct Growth of BiVO4/Bi2S3 Nanorod Array on Conductive Glass as Photocatalyst for Enhancing the Photoelectrochemical Performance. *ACS Appl. Energy Mater.* **2018**, *1*, 6089–6100. [CrossRef]

26. Zheng, Y.; Zheng, L.; Zhan, Y.; Lin, X.; Zheng, Q.; Wei, K. Ag/ZnO heterostructure nanocrystals: Synthesis, characterization, and photocatalysis. *Inorg. Chem.* **2007**, *46*, 6980–6986. [CrossRef]

27. Li, X.H.; Xu, H.Y.; Zhang, X.T.; Liu, Y.C.; Sun, J.W.; Lu, Y.M. Local chemical states and thermal stabilities of nitrogen dopants in ZnO film studied by temperature-dependent x-ray photoelectron spectroscopy. *Appl. Phys. Lett.* **2009**, *95*. [CrossRef]

28. Vattikuti, S.V.P.; Shim, J.; Byon, C. Synthesis, characterization, and optical properties of visible light-driven Bi$_2$S$_3$ nanorod photocatalysts. *J. Mater. Sci. Mater. Electron.* **2017**, *28*, 14282–14292. [CrossRef]

29. Vattikuti, S.V.P.; Shim, J.; Byon, C. 1D Bi2S3 nanorod/2D e-WS2 nanosheet heterojunction photocatalyst for enhanced photocatalytic activity. *J. Solid State Chem.* **2018**, *258*, 526–535. [CrossRef]

30. Zhang, Z.; Xu, R.; Wang, Z.; Dong, M.; Cui, B.; Chen, M. Visible-Light Neural Stimulation on Graphitic-Carbon Nitride/Graphene Photocatalytic Fibers. *ACS Appl. Mater. Interfaces* **2017**, *9*, 34736–34743. [CrossRef] [PubMed]

31. Pearson, R.G. Absolute electronegativity and hardness: Application to inorganic chemistry. *Inorg. Chem.* **1988**, *27*, 734–740. [CrossRef]

32. Yu, L.; Zhang, X.; Li, G.; Cao, Y.; Shao, Y.; Li, D. Highly efficient Bi2O2CO3/BiOCl photocatalyst based on heterojunction with enhanced dye-sensitization under visible light. *Appl. Catal. B Environ.* **2016**, *187*, 301–309. [CrossRef]

33. Cheng, H.; Huang, B.; Dai, Y.; Qin, X.; Zhang, X. One-step synthesis of the nanostructured AgI/BiOI composites with highly enhanced visible-light photocatalytic performances. *Langmuir* **2010**, *26*, 6618–6624. [CrossRef]

Publisher's Note: MDPI stays neutral with regard to jurisdictional claims in published maps and institutional affiliations.